Supporting Information for

A chip-scale oscillation-mode optomechanical inertial sensor near the thermodynamical limits

Yongjun Huang, Jaime Gonzalo Flor Flores*, Ying Li, Wenting Wang, Di Wang, Noam Goldberg, Jiangjun Zheng, Mingbin Yu, Ming Lu, Michael Kutzer, Daniel Rogers, Dim-Lee Kwong, Layne Churchill, and Chee Wei Wong**

E-mail: yongjunh@uestc.edu.cn; jflorflores@ucla.edu; cheewei.wong@ucla.edu

I. Comparisons with state-of-the-art accelerometers

State-of-the-art solid-state accelerometers can be categorized into the following groups: [S1–S30] **(1)** Capacitive sensing[S1-S3] with the proof mass on one side of a parallel plate. This approach involves compensation and amplification circuits to detect minute capacitance changes and translate them into an output voltage. **(2)** Piezoresistive sensing[S4,S5] through mechanical resistive transduction in internal stresses of the support spring. **(3)** Piezoelectric sensing[S6-S8] which provides a direct voltage from the displacement field through the material polarizability. **(4)** Resonant accelerometers[S9,S10] to measure the resonant frequency shift under acceleration. **(5)** Tunneling accelerometers[S11-S13] based on electron tunneling and exponential sensitivity, along with feedback control designs. **(6)** Optical drive, sensing, and readout with coherent laser sources through evanescent-field or resonant cavity transduction,[S14-S17] including the recently developed cavity optomechanical accelerometers.[S18-S24] Gravimeters from Micro-g LaCoste & Scintrex are also cited in Reference [S25], with applications in regional geophysics research, mineral and petroleum exploration, and environmental monitoring. We estimate the bandwidth at 1 to 100 Hz, with the control electronics of the TAGS-6 and MGS-6 at 20 Hz and 1 Hz recording rates respectively.

Most of the referenced accelerometers work by measuring non-constant acceleration, which modulates a carrier signal, and have a large test frequency range. Here we summarize the best resolution performances at the lowest test frequency for all the accelerometers for comparison with current state-of-the-art technologies. **Figure S1** shows a white space map of our design compared with other high-performance accelerometers mentioned above in terms of frequency-resolution tradeoff, which are important metrics for accelerometers. In this figure, the designs falling into the left-bottom region have the better performances, holding high-resolution at lower test frequencies.[21] We also emphasize that our approach is through

resonant driving (different from vibrational sensing) to measure constant and low-frequency accelerations in the bandwidth required for inertial navigation. Our approach offers advantages such as: (1) high-resolution, (2) large dynamic range, as well as (3) direct (RF) frequency readout for chip-scale CMOS RF electronics signal processing, compared to optical signal processing approaches.

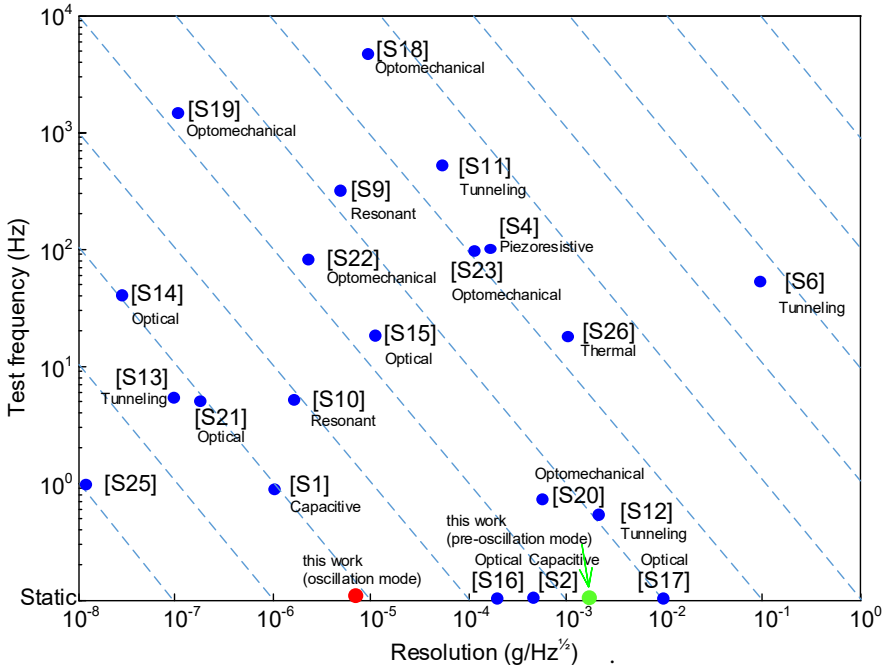

Figure S1. State-of-the-art accelerometer test frequency versus resolution comparisons. Comparisons of our studies to other accelerometers including capacitive, piezoelectric, piezoresistive, resonant, thermal, tunneling, and optical accelerometers in Reference [S1–S26]. The dashed lines depict the tradeoff between test frequency and resolution. *g* denotes the gravitational constant at 9.81 m/s^2.

Table S1 summarizes the resolution (noise density) levels for most of the consumer and industry grade accelerometers used for wide applications including inertial navigation, inclination sensing, platform stabilization, wearable device motion sensing, and condition-based monitoring. It indicates that our experimental demonstrated resolution is comparable to most of the industry grade accelerometers. With further laser detuning optimization and stabilization, the resolution level can be further improved down to 2 μg/Hz$^{1/2}$ (see SI VI.A).

Table S2 summarizes the reported state-of-the-art devices in terms of the test frequency, resolution and bandwidth, thermal limit, dynamic range, resonant frequency, and the readout method. This compares the prior high-frequency optomechanical vibration-shock accelerometers to our low-frequency optomechanical inertial sensor.

Table S1. Performance comparison for current inertial sensors and inertial navigation devices.

Company	Product Type	Resolution sensitivity (noise density)	Bandwidth
Analog Device	ADXL345/355	290 μg/Hz$^{1/2}$	6.25 Hz
	ADcmXL3021	26 μg/Hz$^{1/2}$	100 Hz to 10 kHz
	ADIS16210	190 μg/Hz$^{1/2}$	50 Hz
Lord	3dm-gx5-35/45	25 μg/Hz$^{1/2}$	225 Hz
	3dm-rq1	50 μg/Hz$^{1/2}$	250 Hz
	3dm-gq4-45		
Kionix	KXR94-1071/2283	45 μg/Hz$^{1/2}$	800 Hz
Vectornav	VN-200/300	14 μg/Hz$^{1/2}$	260 Hz
Honeywell	QA2000	70 μg/Hz$^{1/2}$	10 to 500 Hz
Safran Colibrys	HS8030/MS9000	18 μg/Hz$^{1/2}$	none
	MS1000	7 μg/Hz$^{1/2}$	none
This work (chip-scale optomechanical cavity)	Measurements	8.2 μg/Hz$^{1/2}$	100 Hz*
	Theory	≈ 3.2 μg/Hz$^{1/2}$	100 Hz*

*this is the data acquisition rate corresponding to the inverse of integrating time.

Table S2. Performance comparison for optomechanical accelerometers, from vibration-shock to inertial sensing, along with the different readout methods.

Ref.	Test frequency	Resolution sensitivity @ bandwidth	Thermal limit	Dynamic range	Resonant frequency	Readout method
Vibration-shock sensors						
[S18]	5 kHz	10 μg/Hz$^{1/2}$ @ 5-25 kHz	1.4 μg/Hz$^{1/2}$	40 dB	27.5 kHz	optical
[S19]	1.5 kHz	0.1 μg/Hz$^{1/2}$ @ 1.5-10.5 kHz	3 ng/Hz$^{1/2}$	none	10.7 kHz	optical
[S20]	1 kHz	8 μg/Hz$^{1/2}$ @ 1-10 kHz	6.1 ng/Hz$^{1/2}$	none	10.7 kHz	optical
[S21]	5 Hz	0.2 μg/Hz$^{1/2}$ @ 43 Hz*	49.1 ng/Hz$^{1/2}$	none	34.5 Hz	optical
[S23]	2 kHz	40 μg/Hz$^{1/2}$ @ 2-7 kHz	6 μg/Hz$^{1/2}$	95 dB	13.2 kHz	optical
Inertial sensors						
[S22]	83 Hz	4.5 μg/Hz$^{1/2}$ @ 10-100 Hz	0.24 μg/Hz$^{1/2}$	none	133 Hz	optical
This work	Low-freq. (≈ 20 Hz)	8.2 μg/Hz$^{1/2}$ @ 100 Hz*	3.2 μg/Hz$^{1/2}$	43 dB	71.3 kHz	RF

*this is the data acquisition rate corresponding to the inverse of integrating time.

Table S3 shows the potential scaling of our cavity optomechanical accelerometer for increasing motional masses and smaller bandwidth. This increased motional mass is achieved by adding more masses in parallel to the current 5.6-nanogram demonstration. This is first done by adding 20 repeated units, each with their own support springs so as to preserve the mechanical support fabrication yield and the resonant frequency at 71.3 kHz. Subsequently we will increase the mass of each unit, simply by making each motional mass larger, and working with 40 repeated units. Then, we will bring the resonant frequency down to 50 Hz with softer springs k, bringing the thermal-limited resolution sensitivity down to ≈ 2.1

ng/Hz$^{1/2}$. We will stabilize the low-frequency (Hz level) mechanical drifts to allow 10 Hz detection bandwidth. If the low-frequency drifts are well-suppressed, then a potential 0.5 Hz detection bandwidth can be examined, for an ≈ 2.1 ng/Hz$^{1/2}$ thermal-limited resolution sensitivity.

Table S3. Large motional mass and long-integration time performances of the cavity optomechanical inertial sensing.

Motional mass	Resonant frequency	Thermal-limited resolution sensitivity	Bandwidth
5.6 nanograms (this work)	71.3 kHz	3.2 μg/Hz$^{1/2}$	100 Hz
20 × 5.6 nanograms	71.3 kHz (compensated *k*)	≈ 829 ng/Hz$^{1/2}$	100 Hz
40 × 60 nanograms	71.3 kHz (compensated *k*)	≈ 79 ng/Hz$^{1/2}$	100 Hz
40 × 60 nanograms	50 Hz (decreased *k*)	≈ 2 ng/Hz$^{1/2}$	10 Hz
40 × 60 nanograms	50 Hz (decreased *k*)	≈ 2 ng/Hz$^{1/2}$	0.5 Hz

*k = motional mass mechanical stiffness

II. Optomechanical inertial sensor optical, mechanical designs and RF readout

II.A. Inertial sensor optical and mechanical designs

Optomechanical cavities[S31–S36] can be cooled towards or to the quantum mechanical ground state with a red-detuned driving laser[S37–S39] or driven into oscillation mode with a blue-detuned driving laser.[S40–S46] Recent research in cavity optomechanics has led to the demonstration of coupled states,[S47] and quantum transduction or states.[S48–S51] In our subset with the slot-type photonic crystal cavity[S52,S53], the optical cavity modes are designed with MEEP[S54] and mechanical modes are designed with COMSOL Multiphysics. The resulting optical and mechanical modes are illustrated in **Figure S2**.

II.B. Inertial sensor mechanism and model

For an optomechanical system, the coupling rate is defined as $g_{om} = d\omega/dx$.[S53,S55] The spring effect is driven by dynamical backaction, which can be derived from coupled equations of motion[S56] for the optical and mechanical modes. With an external constant acceleration signal applied on the proof mass, we add a corresponding signal force in the vibration equation:

$$\frac{d\hat{a}}{dt} = i\Delta(x)\hat{a} - \left(\frac{1}{2\tau_0} + \frac{1}{2\tau_{ex}}\right)\hat{a} + i\sqrt{\frac{1}{2\tau_{ex}}}s, \tag{S1}$$

$$\frac{d^2x}{dt^2} + \frac{\Omega_m}{2Q_m}\frac{dx}{dt} + \Omega_m^2 x = \frac{F_o(t)}{m_x} + \frac{F_T(t)}{m_x} + \frac{F_s}{m_x}. \tag{S2}$$

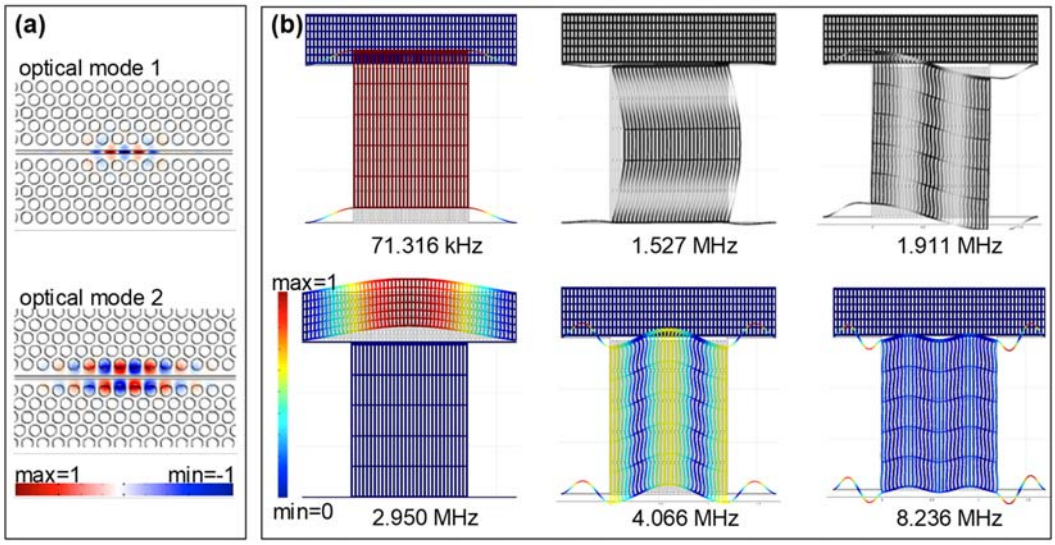

Figure S2. Optomechanical inertial sensor design. a) Modeled transverse-electric field distribution of the two resonant optical modes of the slot cavity. b) Modeled displacement field of the first six mechanical modes of the inertial sensor. The fundamental mode of the proof mass, which is the first deformation field shown, is used to test the acceleration. The corresponding resonant frequencies are listed below each panel. Modes in color can couple to optical mode1 and are symmetric with respect to the *y*-axis. From symmetry, modes in grey are not excited.

The first equation describes the dynamics of the optical field, where $|\hat{a}|^2$ is the stored cavity energy and $1/(2\tau_0)+1/(2\tau_{ex})=1/(2\tau)$ is the optical field decay rate. For an oscillator, a constant applied force will result in an additional displacement shift $x_s=F_s/\Omega^2_m m_x$. The displacement can be written as: $x = x_a + x_{th} + x_s$, where x_a is the solution of the mechanical equation without the constant force and x_{th} the noise due to thermal Brownian motion. For $x = x_o \sin(\Omega_m t) + x_{th} + x_s$, the solution of the coupled equations can be obtained in terms of Bessel functions:

$$\tilde{a}(t) = \hat{a}(t)e^{-i\omega_l t} = \sqrt{\frac{\eta_c}{\tau}} s \sum_{n=-\infty}^{+\infty} \frac{(-i)^n J_n(\beta)}{-i(\omega_l + n\Omega_m - \omega_c + g_{om}x_s) + 1/(2\tau)} e^{-i(\omega_l + n\Omega_m)t + i\beta\cos(\Omega_m t)}, \quad \text{(S3)}$$

where $\beta = g_{om}x_o/\Omega_m$. In our case, detuning $\Delta\ (= \omega_l - \omega_c + g_{om}x_s) >> \Omega_m$ and we obtain the effective frequency as:

$$\Omega'_m = \sqrt{\Omega_m^2 + \left(\frac{2|\hat{a}|^2 g_{om}^2}{((\omega_l - \omega_c + g_{om}x_s)^2 + (1/2\tau)^2)\omega_c m_x} \right)(\omega_l - \omega_c + g_{om}x_s)}, \quad \text{(S4)}$$

Figure S3 illustrates the numerical modeling of the optomechanical transduction rate change with slot widths, as well as the effective optomechanical vibration frequency shift (optomechanical stiffening) for slot width changes.

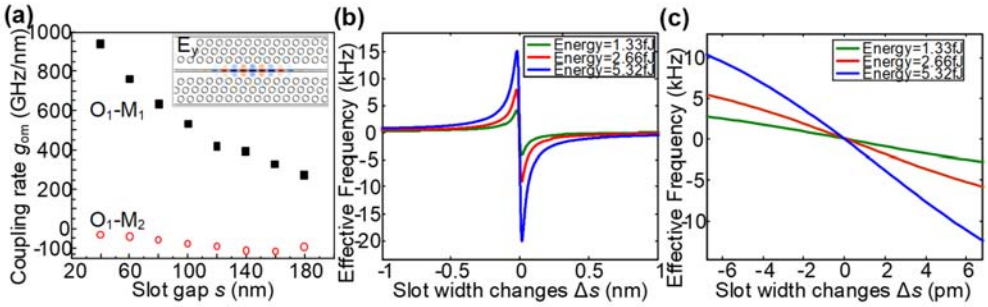

Figure S3. Design of chip-scale inertial sensor frequency shifts. a) Modeled optomechanical coupling rates. Fundamental optical mode coupling with first- (black solid squares) and second- (red open circles) allowed mechanical modes, computed for the different slot width *s*. The inset panel is the E_y-field distribution of the slot inertial sensor. b) Modeled overall RF shift for various sensed slot-cavity gaps *s*, for 1.33 fJ (red), 2.88 fJ (blue), and 5.32 fJ (green) intracavity stored energies. c) Zoom-in of RF frequency shift for slot cavity displacements Δs of ± 6.5 pm.

We derive the linearized form of **Equation (S4)** about a constant frequency $\hat{\omega}_l$, as:

$$\Omega'_m = \sqrt{\Omega_m^2 + \left(\frac{2|\hat{a}|^2 g_{om}^2}{((\hat{\omega}_l-\omega_c)^2+(1/2\tau)^2)\omega_c m_x}\right)(\hat{\omega}_l-\omega_c)} + \frac{|\hat{a}|^2 g_{om}^2((1/2\tau)^2-(\hat{\omega}_l-\omega_c)^2)}{((\hat{\omega}_l-\omega_c)^2+(1/2\tau)^2)^2\omega_c m_x\sqrt{\Omega_m^2+\left(\frac{2|\hat{a}|^2 g_{om}^2}{((\hat{\omega}_l-\omega_c)^2+(1/2\tau)^2)\omega_c m_x}\right)(\hat{\omega}_l-\omega_c)}}(\omega_l-\hat{\omega}_l) \quad (S5)$$

For the resonant mode, in which the displacement x_s is on the order of 10 fm, the product $g_{om}x_s$ is much smaller than the laser detuning. Therefore Ω'_m can be linearized with detuning. Moreover, at the point of zero detuning ($\hat{\omega}_l = \omega_c$), the above equation for Ω'_m further simplifies into:

$$\Omega'_m = \Omega_m + \frac{|\hat{a}|^2 g_{om}^2}{(1/2\tau)^2\omega_c m_x \Omega_m}(\omega_l-\omega_c), \quad (S6)$$

II.C. Conversion from PSD to displacement resolution

To convert the power spectral density to the corresponding displacement noise density, we use the relations between the frequency components of the transmitted optical power modulation and the mechanical motion of the proof mass:[S18,S57,S58]

$$P_m(\Delta=\kappa/2)=(1-T_d)\frac{Q_o}{\omega_o}g_{om}P_{\text{det}}x(\Omega), \tag{S7}$$

Here T_d is the normalized transmission dip shown in **Figure 1c** of the main text, and P_{det} is the optical power reaching the detector. Using the Newport 2117 balanced photodetector with transimpedance gain of $g_{ti} = 49{,}600$ V/m, it corresponds to a voltage output of $V_m = g_{ti}P_m$. This optical sideband can be determined by using an electronic spectrum analyzer (ESA) in units of V_m^2/Z with Z at 50 Ω and illustrating in the instrument dBm/Hz units via the conversion relation:

$$PSD_{\text{ESA}}(\Omega)=10\cdot\log\left[\frac{(g_{ti}P_m(\Omega))^2}{Z}\cdot 10^3\right]. \tag{S8}$$

With the optomechanical coupling rate determined to be 37.1 GHz/nm below, we obtain the displacement noise density shown in left-upper inset of **Figure 2**a in main text, based on Equation (S7) and (S8), which indicates the displacement noise floor of ~ 0.2 fm/Hz$^{1/2}$ and for the on-resonance fundamental mechanical mode.

The measured RF PSD in a larger frequency band is shown in **Figure S4** with the converted displacement resolution results shown in the right axis. The corresponding mechanical displacement field profiles are shown in the inset of **Figure S4**.

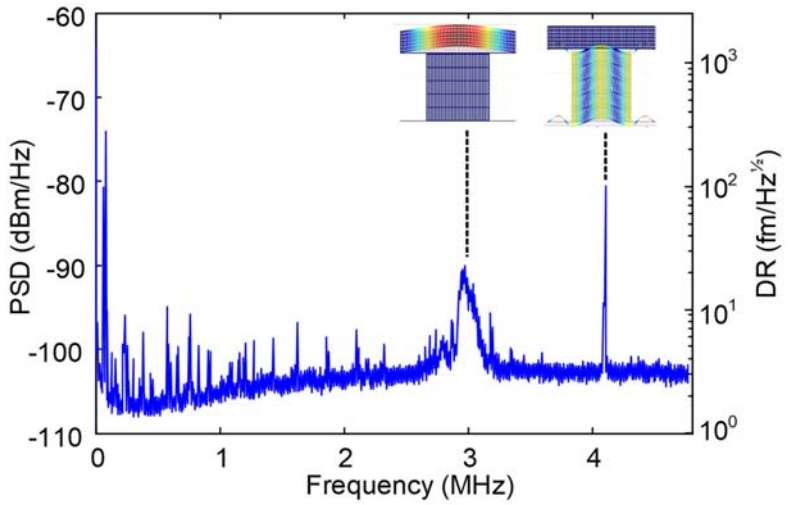

Figure S4. The second two coupled modes at 2.95 MHz and 4.10 MHz, respectively, along with the modeled displacement profiles in the top insets.

II.D. 2D mechanical PSD with detuning at different drive powers

Figure S5 illustrates the measured 2D RF spectra with different laser wavelengths and powers to study the optomechanical stiffening and damping of the inertial sensor. Four sets of complete results are measured with incident powers of 2.8 μW, 8.8 μW, 14 μW, and 22 μW

respectively. From the 2D RF maps, we also fit the RF shift as a function of laser-cavity detuning $\Delta_o|_{xs=0}=\omega_l-\omega_0$ using Equation (S4); this fitting indicates a $g_{om}/2\pi \approx 37.1$ GHz/nm. We should note that the estimated coupling rate matches the demonstration of g_{om} with common phase EOM calibration.[S58]

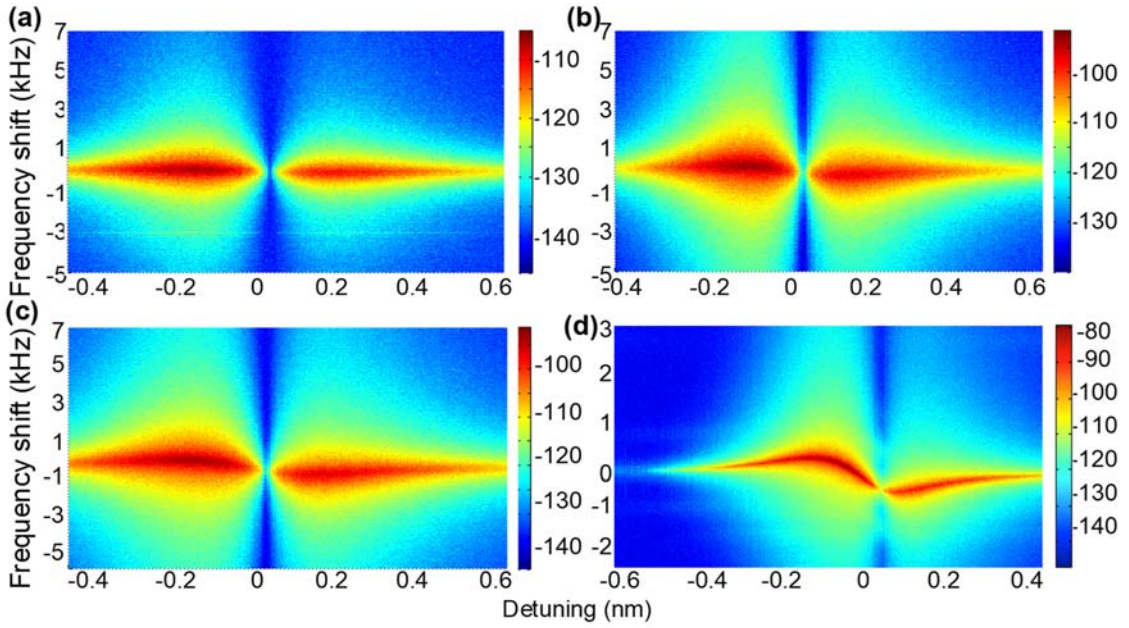

Figure S5. Measured 2D RF spectra for different input powers. The mechanical sensing frequency and linewidth changes with detunings are illustrated for different input powers of a) 2.8 μW, b) 8.8 μW, c) 14 μW, and d) 22 μW. The optical cavity linewidth is 350 pm or a cavity decay rate Γ of 43 GHz. When the detuning is large or the input power is lower than 2.8 μW, the RF spectrum represents the proof mass eigenfrequency at 71.3 kHz, in this device. With increased input pump power, optomechanical damping and spring effects are observed. From these measurements, g_{om} is determined to be 37.1 GHz/nm.

III. Acceleration sensing with rotary stage and estimates of measurement uncertainties

III.A. Measurement setup

The tested device, the nanopositioning stages, and the tapered fiber are placed inside a customized Janis ST-500 vacuum chamber for the measurements. Measured devices are placed under the vacuum chamber imaging window, which allows us to image and control the tapered fiber coupling to the device. A 5-axis Attocube positioners translate the devices over a 5 mm travel range with sub-nanometer scanning resolution in fine-positioning mode. The prepared tapered fibers have a 90% transmission. It is connected with the drive laser and detector outside the vacuum chamber through Teflon fiber feedthroughs. An Edwards T-

Station 75 turbopump evacuates the chamber to high vacuum. The pumping station consists of an E2M1.5 backing pump and a XDD1 turbo pump, allowing the chamber to reach a 10^{-7} torr pressure. A conventional tunable laser is used for most of the measurements. For the low noise PSD measurements such as the grey line in Figure 3f, a narrow-linewidth laser is used.

III.B. Estimates of measurement uncertainties

We have considered the error from misalignment between the device mounting and the acceleration direction. If there is an error angle θ between the device mounting and acceleration direction, the acceleration error is $\triangle a = a - a' = (1-\cos\theta)a$. Therefore, even if there is a ±5° misalignment, the error in the acceleration estimate $\Delta a/a$ would only be (1-cos5°) or equivalently a ±0.38% fixed (and consistent) offset in the imparted acceleration in the measurement. **Figure S6** also shows the 2D RF spectra with the device mounted in the 180° direction opposite from **Figure 3**a (i.e. acceleration in the *–y* axis direction). The imparted acceleration ranges from 6.5 mg to 122.1 mg. The observed RF shift is estimated ≈ +50 Hz, through a numerical fit to the experimental data. The overall detection sensitivity is determined at ≈ 2.29 mg/Hz.

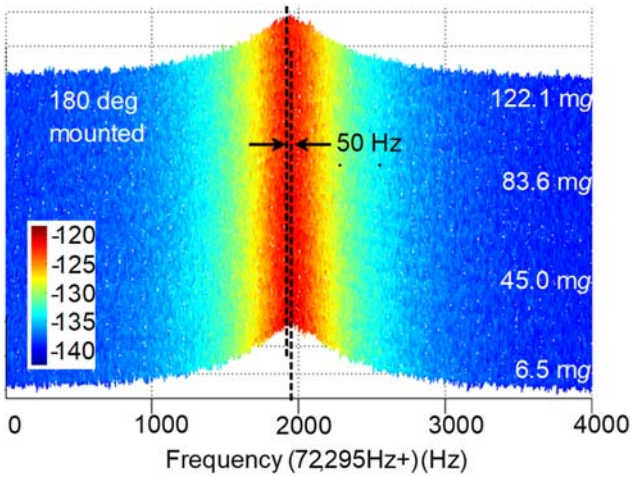

Figure S6. Backaction RF transduction with inertial sensor mounted in 180° direction without the oscillation mode, for acceleration in the *-y* direction. Imparted acceleration from 6.5 mg to 122.1 mg, with a corresponding RF shift of ≈ +50 Hz. The overall detection sensitivity is determined at ≈ 2.29 mg/Hz.

In addition, the effects of pump laser wavelength instability and coupled intracavity energy instability can be considered through **Equation (1)** of the main text. The tunable Santec laser (TSL-510C) has specified wavelength and power instabilities of less than ± 166 fm and ± 0.0017 dB in 10-minutes, operated free-running and with internal feedback[S56]

control. The wavelength instabilities translate into ± 5% uncertainty for the measured acceleration resolution. The low optical Q (and relatively large optical linewidth of ≈ 1 nm) reduces the sensitivity to pump wavelength fluctuations, although wavelength feedback-locking to an external frequency reference can further drive down this uncertainty. The ± 0.0017-dB 10-minute power instability is negligible in the RF readout.

IV. Inertial sensor sensitivity

The proof mass is supported by thin tethers and acts as an oscillator. The scale factor of an inertial sensor is defined as the RF shift responding to a unit acceleration change, $\Delta\Omega / \Delta a$. Acceleration sensitivity in terms of displacement can be calculated from the mechanical susceptibility:

$$| x(\Omega) | = | \chi(\Omega) | \cdot a(\Omega) = \left| \frac{1}{\Omega_m^2 - \Omega^2 + i\Omega\Omega_m / Q_m} \right| \cdot (a_o(\Omega) + a_{th} + a_{DC}) . \qquad \text{(S9)}$$

Here $a_o(\Omega)$, a_{th} and a_{DC} correspond to the optical gradient force, thermal noise and external force respectively, which can be obtained from Equation (S2). The oscillator operates at its resonant frequency for low-frequency accelerations; therefore, we obtain $\Delta|x(\Omega)| / \Delta a_{DC} = |\chi(\Omega)| = 1/\Omega_m^2$. Then, the cavity resonance frequency is a function of slot width x, which is used to detect the position of the proof mass, and corresponds to the fitted optomechanical coupling. As a result, the mechanical resonant frequency shift under various accelerations at the fixed drive wavelength can be described as:

$$\Omega_m^{'} = \sqrt{\Omega_m^2 + \left(\frac{2|\hat{a}|^2 g_{om}^2}{((\omega_l - \omega_c + g_{om}x_s)^2 + (1/2\tau)^2)\omega_c m_x} \right)(\omega_l - \omega_c + g_{om}x_s)} , \qquad \text{(S10)}$$

in both pre-oscillation and oscillation modes. The equation is the same as Equation (S4) and reiterated here. We note that thermal noise does not affect the scale factor (sensitivity) as mentioned in Reference [S20].

V. Frequency instability and acceleration resolution

Here we measure the Allan deviation of the inertial sensor by using frequency counting (Hewlett-Packard 5351A) to characterize the frequency fluctuation for the pre-oscillation and oscillation modes as shown in **Figure S7**a. It shows the inertial sensor has a fractional frequency instability ($\delta\Omega_0/\Omega_c$, where Ω_c is the carrier frequency) at 7.9×10^{-5} and 3.8×10^{-6} at 10 ms integration time, for the pre-oscillation and oscillation states respectively. In pre-oscillation state, this is equivalent to a noise-limited minimal detectable RF shift $\delta\Omega_m/2\pi$ of 6.9 Hz in 0.01 second integration time. These measurements are performed in vacuum (≈ 10^{-6}

torr). Phase noise is another characterization of the oscillator[S45] and **Figure S7**b illustrates the single sideband phase noise, following the Leeson model characteristics. Fitted with piecewise functions, the resulting corner frequency is 3.8 kHz and a $1/f^3$ region is observed between ≈ 100 Hz to 1 kHz offsets. After the corner frequency the $1/f^2$ region arises from white frequency noise. At 10 kHz offset, the phase noise is determined down to about -102-dBc/Hz for the ≈ 70 to 80 kHz oscillator.

As discussed in Reference [39] of the main text, the frequency noise density can be easily calculated from the measured phase noise in Laplace domain. The oscillator output is a sinusoidal signal $v(t)=A_0\sin(\omega_0 t+\varphi(t))$, and the instantaneous frequency $f(t)$ can be defined as $f(t)=\omega_0/2\pi+\varphi'(t)/2\pi$. Therefore the frequency noise term should be $\Delta f(t)=\varphi'(t)/2\pi$ and can be transferred to Laplace domain, $S_f=f^2S_\varphi$, where S_f and S_φ are the frequency noise density (in units of Hz^2/Hz) and phase noise density (in units of dBc/Hz). With the measured frequency instability results, the inertial sensor noise can be obtained by multiplying the frequency noise with the measured sensitivity. The obtained inertial sensor resolution is determined to be 1.8 $mg/Hz^{1/2}$ for pre-oscillation mode and 8.2 $\mu g/Hz^{1/2}$ for oscillation mode, both at 10-ms integration times.

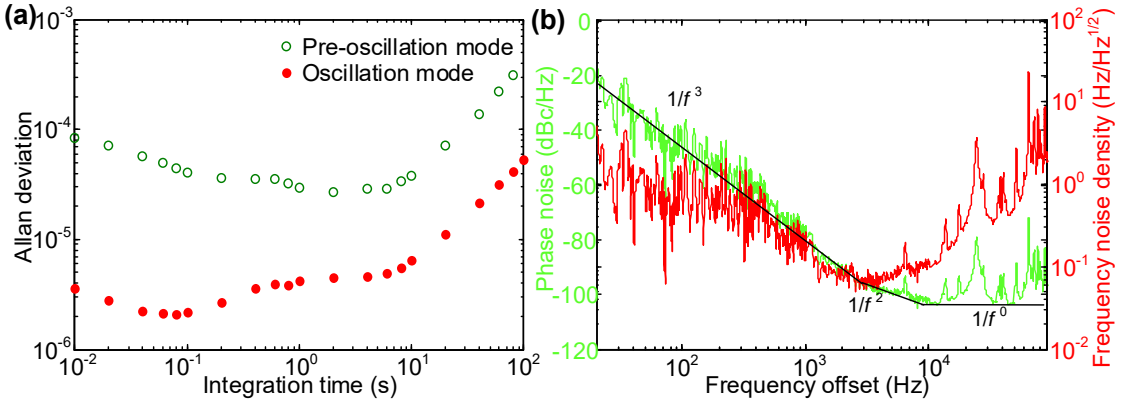

Figure S7. Pre-oscillation and oscillation mode characteristics of the optomechanical inertial sensor. a) Allan deviation measurements for the frequency tone output of the inertial sensor at pre-oscillation and oscillation modes. These data are carried out by frequency counter (Hewlett-Packard 5351A), which shows the levels of 7.9×10^{-5} and 3.8×10^{-6} at 10 ms integration, for the pre-oscillation and oscillation states respectively. b) Phase noise measurements S_φ of the oscillation mode. The green curve shows experimental data. The black lines indicate the fitted $1/f^3$, $1/f^2$ and $1/f^0$ dependences. The red line on the right vertical axis is the corresponding frequency noise density S_f ($=f^2 S_\varphi$).

VI. Inertial sensor resolution - noise equivalent acceleration and noise contributions

VI.A. Thermal noise

The inertial sensor resolution is defined by its noise equivalent acceleration. This noise comes primarily from thermal Brownian motion. Noise from thermal Brownian motion corresponds to the thermomechanical fluctuations and is discussed below. We start with the evaluation of minimum detectable frequency:[S30,S60]

$$\delta\Omega_{th} = \left[\int_{\Omega_m - \pi\Delta f}^{\Omega_m + \pi\Delta f} S_{\Omega\Omega}^{th}(\Omega) d\Omega \right]^{1/2}, \tag{S11}$$

where

$$S_{\Omega\Omega}^{th}(\Omega) \approx \frac{\Omega_m^5}{Q_m^3} \frac{k_B T}{E_C} \frac{1}{(\Omega^2 - \Omega_m^2)^2 + \Omega^2 \Omega_m^2 / Q_m^2} = \frac{\Omega_m^5}{Q_m^3} \frac{k_B T}{E_C} |\chi(\Omega)|^2 . \tag{S12}$$

Here $E_C = m_x \Omega_m^2 \langle x_c^2 \rangle$ represents the maximum energy in the oscillator and $\langle x_c \rangle$ is the constant mean square amplitude. Under the conditions of $Q_m >> 1$ and $2\pi\Delta f << \Gamma_m$ ($=\Omega_m/Q_m$), the integration of Equation (S12) can be approximated to:

$$\delta\Omega_{th} = \left[\frac{k_B T}{E_C} \frac{\Omega_m \Delta f}{Q_m} \right]^{1/2} . \tag{S13}$$

The ratio of maximum energy, E_C, to the thermal energy, $E_{th}=k_B T$ gives the dynamic range intrinsic to the cavity optomechanical oscillator and relates to the signal-to-noise ratio:[S30]

$$\text{SNR (dB)} = 10 \log(E_C / k_B T). \tag{S14}$$

Therefore Equation (S13) can be revised as:

$$\delta\Omega_{th} = \left[10^{(-SNR/10)} \frac{\Omega_m \Delta f}{Q_m} \right]^{1/2} . \tag{S15}$$

From the measured thermal frequency fluctuations, the thermally-limited acceleration detection at different laser detunings can be obtained as:

$$a_{th} = S \cdot \delta\Omega_{th} \cdot \sqrt{t_{meas}} = S \cdot \left[10^{(-SNR/10)} \frac{\Omega_m \Delta f}{Q_m} \right]^{1/2} \cdot \sqrt{t_{meas}} . \tag{S16}$$

Figure S8 illustrates the calculated thermal acceleration detection at different optical detunings, for both pre-oscillation and oscillation states. Here the sensitivity is calculated with a small external acceleration change (≈ 0.1 mg), and the thermal frequency fluctuation is assumed unchanged at different detunings. Moreover, the SNR and intrinsic mechanical quality Q_m values used are 18 dB and 1383 for pre-oscillation mode. The SNR for the oscillation mode is 70 dB. The measured frequency instability shown in **Figures S7** matches the theoretical prediction (Equation S16) obtained here.

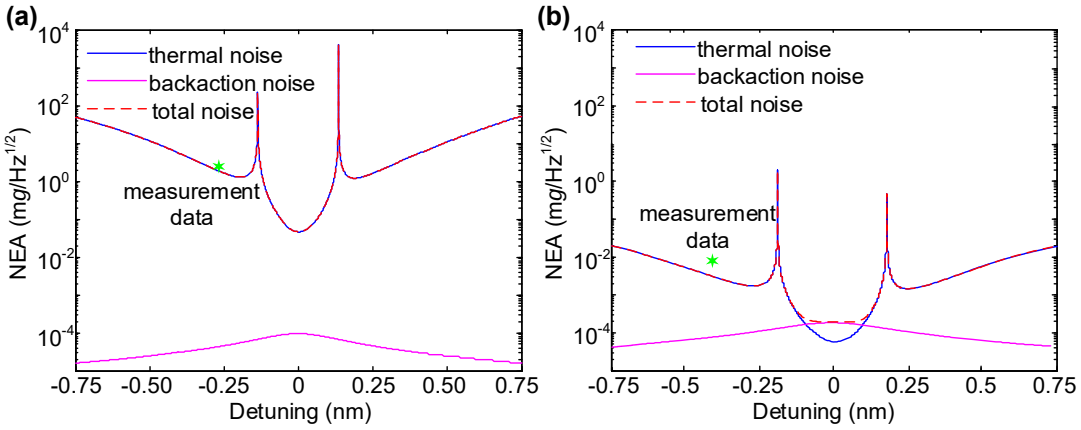

Figure S8. Theoretical calculations of noise equivalent acceleration for both pre-oscillation and driven oscillation modes. a) Pre-oscillation mode. b) Driven-oscillation mode.

VI.B. Quantum backaction noise

Optical noise arising from quantum backaction noise a_{BA} exerts a random force on the mechanical oscillator. The acceleration noise created by optomechanical backaction is:

$$S_{aa}^{BA} = 2\frac{(\hbar g_{om})^2}{m_x^2} n_c \frac{4}{\kappa}, \tag{S17}$$

where n_c is the cavity photon number. When the input power is 200 μW for oscillation, the photon number in the cavity is ≈ 2,644 at zero detuning and the above equation results in a noise equivalent acceleration from quantum backaction as: $a_{BA} = \sqrt{S_{aa}^{BA}} \approx 184$ ng/Hz$^{1/2}$ at zero detuning. The calculated quantum backaction noise across full optical detuning range is shown in **Figure S8**.

Conventional frequency spectrum analyzers, instead of frequency counting, can bring large imprecision to the acceleration measurements. Readout frequency accuracy of a frequency spectrum analyzer (such as the Agilent PSA E4448a) is determined by the sum of several error sources, including frequency reference inaccuracy, span error, and resolution bandwidth (RBW) center-frequency error. Frequency reference accuracy is ± [(time since last adjustment × aging rate) + temperature stability + calibration accuracy] = ± [1×10^{-7}/year × 1 year + 1×10^{-8} + 7×10^{-8}] = $\pm1.8 \times 10^{-7}$. For the measurement, the span error is 0.25% × span = 0.25% × 400 Hz = 1 Hz and RBW error is 5% × RBW = 5% × 1 Hz = 50 mHz, or a total of 3.05 Hz imprecision, if a conventional spectral analyzer is used instead of frequency counting.

VII. Detection dynamic range

We also examined the linear response range of the inertial sensor. **Figure S9**a illustrates the computed linear response dynamic range from optomechanical stiffening. With increase in

the acceleration, the frequency shift deviates from linearity due to the nonlinear dependence of the optical resonance on the slot width *s*. To compare with measurements, the linearly of the mechanical shift range is defined as $10\log(a_l\text{-}a_{min})/a_{min}$), where a_l stands for the acceleration value in which the frequency fluctuates from the linearity (<0.05% standard deviation) and a_{min} the minimum detectable acceleration in oscillation mode, which illustrates a ≈ 44.8 dynamic range. We also calculated the dynamic range versus stored energy for devices with different proof masses. As illustrated in **Figure S9**b, linear dynamic range increases with stored energy but decreases with larger proof masses. The corresponding experimental dynamic range is determined to be 43 dB and illustrated in **Figure S9**b, matching well with our numerical modeling predictions. Follow-up devices have shown sizably larger dynamic range.

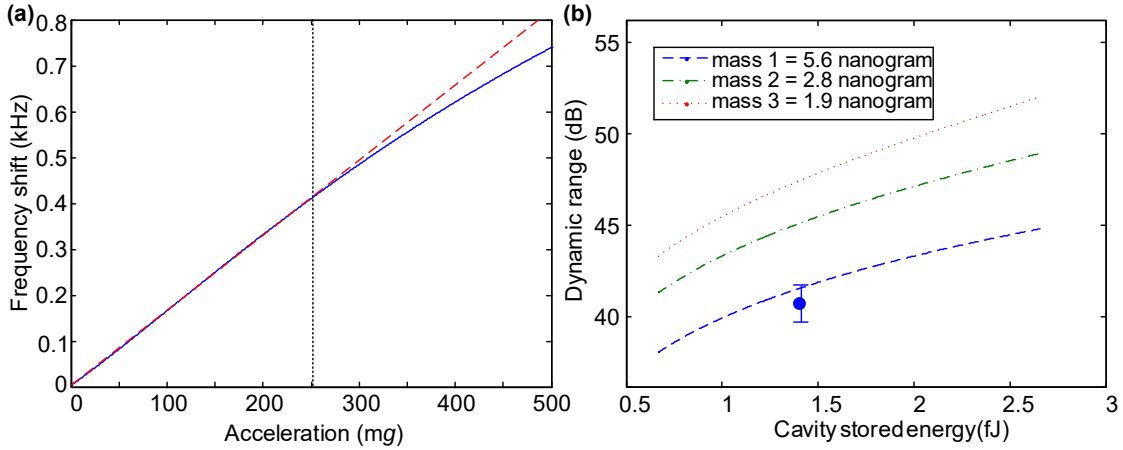

Figure S9. Dynamic range parameter space of the optomechanical inertial sensor. a) Modeled primary inertial sensor design with ≈ 44.8 dB dynamic range. Dashed red line shows the linear dependence, and blue line represents the modeled frequency shift for large imparted accelerations. b) Dynamic range for increasing optical pump power (stored intracavity energy) and different proof masses. The experimental dynamic range from the measurement data analysis is determined as 43 dB with the represented solid blue datapoint.

Supporting references

[S1] F. Rudolf, A. Jornod, J. Bergqvist, H. Leuthold, *Sensors and Actuators A: Physical* **1990**, *21*, 297.

[S2] K. H.-L. Chau, S. R. Lewis, Y. Zhao, R. T. Howe, S. F. Bart, R. G. Marcheselli, *Sensors and Actuators A: Physical* **1996**, *54*, 472.

[S3] C. Acar, A. M. Shkel, *J. Micromech. Microeng.* **2003**, *13*, 634.

[S4] A. Partridge, J. K. Reynolds, B. W. Chui, E. M. Chow, A. M. Fitzgerald, L. Zhang, N. I. Maluf, T. W. Kenny, *J. Microelectromech. Sys.* **2000**, *9*, 58.

[S5] W.-T. Park, A. Patrick, R. N. Chandler, V. Ayanoor-Vitikkate, G. Yama, M. Lutz, T. W. Kenney, *J. Microelectromech. Syst.* **2006**, *15*, 507.

[S6] D. L. DeVoe, A. P. Pisano, presented at IEEE Solid-State Sensors and Actuators (Transducers'97), Chicago, USA, June 16-19, **1997**.

[S7] S. C. Masmanidis, R. B. Karabalin, I. De Vlaminck, G. Borghs, M. R. Freeman, M. L. Roukes, *Science* **2007**, *317*, 780.

[S8] S. Tadigadapa, K. Mateti, *Meas. Sci. Technol.* **2009**, *20*, 092001.

[S9] A. A. Seshia, M. Palaniapan, T. A. Roessig, R. T. Howe, R. W. Gooch, T. R. Schimert, S. Montague, *J. Micromechanical Sys.* **2002**, *11*, 784.

[S10] X. Zou, P. Thiruvenkatanathan, A. A. Seshia, *J. Microelectromech. Syst.* **2014**, *23*, 768.

[S11] R. L. Kubena, G. M. Atkinson, W. P. Robinson, F. P. Stratton, *IEEE Electron Device Lett.* **1996**, *17*, 306.

[S12] C. Yeh, K. Najafi, *J. Microelectromech. Sys.* **1998**, *7*, 6.

[S13] C.-H. Liu, T. W. Kenny, *J. Micromechanical Sys.* **2001**, *10*, 425.

[S14] N. C. Loh, M. A. Schmidt, S. R. Manalis, *J. Microelectromech. Sys.* **2002**, *11*, 182.

[S15] P. F. da Costa Antunes, H. F. T. Lima, N. J. Alberto, et al. *IEEE Sensors Journal* **2009**, *9*, 1347.

[S16] K. Zandi, J. A. Bélanger, Y. A. Peter, *J. Microelectromech. Sys.* **2012**, *21*, 1464.

[S17] J. Li, G. Y. Wang, J. N. Sun, et al. *IEEE Photon. Techno. Lett.* **2017**, *29*, 1836.

[S18] A. G. Krause, M. Winger, T. D. Blasius, Q. Lin, O. Painter, *Nature Photon.* **2012**, *6*, 768.

[S19] F. G. Cervantes, L. Kumanchik, J. Pratt, J. Taylor, *Appl. Phys. Lett.* **2014**, ***104***, 221111.

[S20] O. Gerberding, F. Guzmán Cervantes, J. Melcher, J. R. Pratt, J. M. Taylor, *Metrologia* **2015**, *52*, 654.

[S21] Q. Lu, J. Bai, K. Wang, S. He, *J. Microelectromech. Syst.* **2017**, *26*, 859.

[S22] Y. L. Li, P. F. Barker, *Journal of Lightwave Technology* **2018**, *36*, 3919.

[S23] Y. L. Li, P. F. Barker, *Sensors* **2018**, *18*, 4184.

[S24] D. N. Hutchison, S. A. Bhave, presented at 2012 IEEE Micro Electro Mechanical Systems (MEMS), Paris, France, January 29-February 2, **2012**.

[S25] Micro-*g* LaCoste & Scintrex FG5-X with specified precision at 15 uGal/$Hz^{1/2}$ (980 Gal equals to 1 *g*).

[S26] A. M. Leung, J. Jones, E. Czyzewska, J. Chen, B. Woods, presented at IEEE Micro Electro Mechanical Sys. (MEMS '98), Heidelberg, Germany, January 25-29, **1998**.

[S27] K. L. Ekinci, M. L. Roukes, *Rev. Sci. Instr.* **2005**, *76*, 061101.

[S28] A. N. Cleland, M. L. Roukes, *J. Appl. Phys.* **2002**, *92*, 2758.

[S29] S. D. Senturia, Microsystem Design (Kluwer Academic Publishers, New York, 2002).

[S30] K.L. Ekinci, Y.T. Yang, M.L. Roukes, *J. Appl. Phys.* **2014, *95***, 2682.

[S31] M. Aspelmeyer, T. J. Kippenberg, F. Marquardt, *Reviews of Modern Physics* **2014**, *86,*1391.

[S32] I. Favero, K. Karrai, *Nature Photonics* **2009**, *3*, 201.

[S33] D. V. Thourhout, J. Roels, *Nature Photonics* **2010**, *4*, 211.

[S34] M. Li, W. H. P. Pernice, C. Xiong, T. Baehr-Jones, M. Hochberg, H. X. Tang, *Nature* **2008**, *456*, 480.

[S35] G. Bahl, M. Tomes, F. Marquardt, T. Carmon, *Nature Phys*. **2012**, *8*, 203.

[S36] E. Gavartin, P. Verlot, T. J. Kippenberg, *Nature Communications* **2013**, *4*, 2860.

[S37] T. Rocheleau, T. Ndukum, C. Macklin, J. B. Hertzberg, A. A. Clerk, K. C. Schwab, *Nature* **2010**, *463*, 72.

[S38] J. D. Teufel, T. Donner, D. Li, J. W. Harlow, M. S. Allman, K. Cicak, A. J. Sirois, J. D. Whittaker, K. W. Lehnert, R. W. Simmonds, *Nature* **2011**, *475*, 359.

[S39] A. Schliesser, R. Riviere, G. Anetsberger, O. Arcizet, T. J. Kippenberg, *Nature Phys.* **2008**, *4*, 415.

[S40] S. Tallur, S. Sridaran, S. A. Bhave, *Opt. Express* **2011**, *19*, 24522.

[S41] A. B. Matsko, A. A. Savchenkov, L. Maleki, *Opt. Express* **2012**, *20*, 16234.

[S42] P. B. Deotare, I. Bulu, I. W. Frank, Q. Quan, Y. Zhang, R. Ilic, M. Loncar, *Nature Communications* **2012**, *3*, 846.

[S43] J. Li, H. Lee, K. J. Vahala, *Nature Communications* **2013**, *4*, 2097.

[S44] T. Beyazoglu, T. O. Rocheleau, K. E. Grutter, A. J. Grine, M. C. Wu, C. T.-C. Nguyen, presented at IEEE Micro Electro Mechanical Systems (MEMS), Estoril, Portugal, January 26-30, **2014**.

[S45] X. Luan, Y. Huang, Y. Li, J. F. McMillan, J. Zheng, S.-W. Huang, P.-C. Hsieh, T. Gu, D. Wang, A. Hati, D. A. Howe, G. Wen, M. Yu, G. Lo, D.-L. Kwong, C. W. Wong, *Sci. Rep.* **2014**, *4*, 6842.

[S46] K. Fong, M. Poot, X. Han, H. Tang, *Phys. Rev. A* **2014**, *90*, 023825.

[S47] A. H. Safavi-Naeini, T. P. Mayer Alegre, J. Chan, M. Eichenfield, M. Winger, Q. Lin, J. T. Hill, D. E. Chang, O. Painter, *Nature* **2011**, *472*, 69.

[S48] S. Camerer, M. Korppi, A. Jöckel, D. Hunger, T. W. Hänsch, P. Treutlein, *Phys. Rev. Lett.* **2011**, *107*, 223001.

[S49] J. Bochmann, A. Vainsencher, D. D. Awschalom, A. N. Cleland, *Nature Phys.* **2013**, *9*, 712.

[S50] A. H. Safavi-Naeini, S. Groblacher, J. T. Hill, J. Chan, M. Aspelmeyer, O. Painter, *Nature* **2013**, *500*, 185.

[S51] B. D. Clader, *Phys. Rev. A* **2014**, *90*, 012324.

[S52] J. Zheng, Y. Li, N. Goldberg, M. McDonald, A. Hati, M. Lu, S. Strauf, T. Zelevinsky, D. A. Howe, C. W. Wong, *Appl. Phys. Lett.* **2013**, *102*, 141117.

[S53] Y. Li, J. Zheng, J. Gao, J. Shu, M. S. Aras, C. W. Wong, *Opt. Express* **2010***, 18*, 23844.

[S54] A. F. Oskooi, D. Roundyb, M. Ibanescua, P. Bermelc, J.D. Joannopoulosa, S. G. Johnson, *Computer Physics Comm.* **2010**, *181*, 687.

[S55] S. G. Johnson, M. Ibanescu, M. A. Skorobogatiy, O. Weisberg, J. D. Joannopoulos, Y. Fink, *Phys. Rev. E* **2002**, *65*, 066611.

[S56] H. A. Haus, Waves and Fields in Optoelectronics (Prentice Hall, Englewood Cliffs, New Jersey, **1984**).

[S57] A. H. Safavi-Naeini, J. Chan, J. T. Hill, S. Gröblacher, H. Miao, Y. Chen, M. Aspelmeyer, O. Painter, *New Journal of Physics* **2013**, *15*, 035007.

[S58] J. D. Cohen, S. M. Meenehan, O. Painter, *Opt. Express* **2013**, *21*, 11227.

[S59] M. L. Gorodetksy, A. Schliesser, G. Anetsberger, S. Deleglise, T. J. Kippenberg, *Opt. Express* **2010**, *18*, 23236.

[S60] X. L. Feng, C. J. White, A. Hajimiri, M. L. Roukes, *Nature Nano.* **2008**, *3*, 342.